Research Article

Hui-Shen Shen* and Chong Li

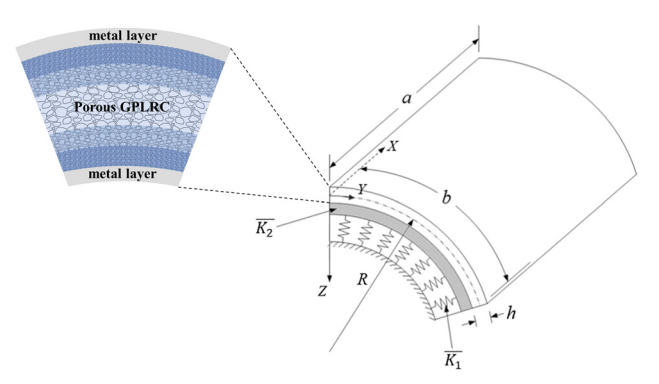
Re-examination of nonlinear vibration and nonlinear bending of porous sandwich cylindrical panels reinforced by graphene platelets

https://doi.org/10.1515/ntrev-2022-0544 received February 7, 2023; accepted April 4, 2023

Abstract: This article re-examines the nonlinear vibration and nonlinear bending responses of porous sandwich cylindrical panels reinforced by graphene platelets resting on elastic foundations in thermal environments. The graphene platelet-reinforced composite (GPLRC) core is assumed to be of multilayers, and each layer may have different porosity coefficient values to achieve a piece-wise functionally graded pattern. By introducing an inhomogeneous model instead of the equivalent isotropic model (EIM), the Young's moduli along with the shear modulus of the porous GPLRC core are predicted through a generic Halpin-Tsai model in which the porosity is included. The thermomechanical properties of metal face sheets and the porous GPLRC core are assumed to be temperature-dependent. Governing equations of motion for sandwich cylindrical panels with porous GPLRC core are formulated based on Reddy's third-order shear deformation theory coupled with von Kármán nonlinear straindisplacement relationships. In the modeling, the panel-foundation interaction and the thermal effects are also considered. The analytical solutions for the nonlinear vibration and nonlinear bending problems are obtained by applying a two-step perturbation approach. Numerical studies are performed to compare the results obtained from the present model and the EIM. The results confirm that the EIM is not suitable for linear free vibration analysis of sandwich cylindrical panels with the porous GPLRC core, but the EIM may be valid for the cases of nonlinear vibration and nonlinear bending analyses of the same panel resting on Pasternak elastic foundations.

Keywords: porous material, graphene platelets, sandwich cylindrical panel, functionally graded, temperature-dependent

Chong Li: School of Aeronautics and Astronautics, Shanghai Jiao Tong University, Shanghai 200240, China



Graphical abstract

1 Introduction

Porous materials are realized as a new class of advanced engineering materials characterized by low density, electrical conductivity, great energy absorption capability, and thermal resistance [1-4]. However, the presence of porosities in the metal matrix will lead to a significant reduction in terms of structural stiffness [5-8]. With the development of nanotechnology and additive manufacturing technology [9,10], nanofillers such as carbon nanotubes (CNTs) [11] or graphene platelets (GPLs) [12] can be added into porous metal foams to increase the stiffness of porous metal materials while maintaining the lightweight nature of foams. GPL can be regarded as an isotropic solid, which consists of a large number of stacked monolayer graphene. GPL-reinforced porous metal foams may be created as particle-reinforced composites where GPLs are uniformly or randomly dispersed in the porous metal foams. The mechanical performance of the porous metal materials reinforced by GPLs may be enhanced substantially while maintaining the lightweight advantage of the porous metal materials.

Many studies have been carried out on the static and dynamic analyses of porous GPL-reinforced composite (GPLRC) flat panels without or with face sheets [13–24]. However, relatively few studies have been done on the static and dynamic analyses of porous GPLRC cylindrical

^{*} Corresponding author: Hui-Shen Shen, School of Aeronautics and Astronautics, Shanghai Jiao Tong University, Shanghai 200240, China, e-mail: hsshen@sjtu.edu.cn

panels. In order to enhance the mechanical performance of porous metal panels, it is an effective approach to incorporate the functionally graded (FG) material concept [25] into the design of the porous metal panel. Zhou et al. [26] investigated vibration and flutter characteristics of porous FG-GPLRC cylindrical panels subjected to supersonic flow based on Reddy's third-order shear deformation theory (TSDT) and by applying the standard Lagrange procedure. Similar to the flat panels, the porous GPLRC cylindrical panels cannot be used as structural components directly in engineering practice. It is a better way to add two face sheets on the outer and inner surfaces of the porous GPLRC layer to create a sandwich panel where the porous GPLRC layer is treated as a hard core, and in that case the Reddy's TSDT is still valid. Twinkle and Pitchaimani [27,28] studied the effects of grading, porosity, and non-uniform edge loads on the natural frequency and buckling load of porous FG-GPLRC cylindrical panels and sandwich cylindrical panels with the porous FG-GPLRC core based on the higher-order shear deformation theory (HSDT) and by applying the Galerkin method. Sun et al. [29] calculated free vibration frequencies of sandwich cylindrical panels with the porous FG-GPLRC core based on the Love shell theory and by applying the Ritz method. In the aforementioned works, the equivalent isotropic model (EIM) was adopted to determine the equivalent Young's modulus of the GPLRC layer through a modified Halpin-Tsai model and the shear modulus is assumed to be related to the Young's modulus by a well-known formula of isotropic material.

It has been reported that, even for the GPLRC flat panel without porosity, the shear modulus will be underestimated by using the EIM [30]. Shen and his co-authors [31,32] proposed an inhomogeneous model instead of the EIM and re-examined the linear and nonlinear vibration and the nonlinear bending along with the buckling and postbuckling responses of porous sandwich plates reinforced by GPLs. They found that the shear modulus is overestimated when the porosity coefficient is less than 0.2, while underestimated when the porosity coefficient is greater than 0.25 by using the EIM. Their results reveal that, owing to the shear modulus effect, for most cases, the difference in the natural frequencies between the two models is over 30%. The nonlinear free vibration frequency amplitude curves, the nonlinear bending load-deflection curves, and the thermal postbuckling load-deflection curves are always underestimated, while the compressive postbuckling equilibrium paths of the porous sandwich plates are always overestimated by using the EIM. Only in the case of porous sandwich plates resting on Pasternak elastic foundations with sufficiently large foundation stiffnesses, the difference between the two models may be negligible, and the EIM may be valid in the analysis.

The purpose of this article is to evaluate the appropriateness of applying the EIM in vibration and bending analyses of porous GPLRC cylindrical panels. We re-examine the nonlinear vibration and the nonlinear bending of sandwich cylindrical panels with metal face sheets and porous GPLRC core resting on elastic foundations in thermal environments. We choose two kinds of porous GPLRC core in the present study, i.e., uniformly distributed (UD) and piecewise FG patterns. The material properties of both metal face sheets and porous GPLRC core are assumed to be temperature-dependent. The novelty of this study is that an inhomogeneous model is introduced instead of the EIM for the porous GPLRC core, where the Young's moduli along with the shear modulus are predicted through a generic Halpin-Tsai model in which the porosity is included. Governing equations of motion for porous sandwich cylindrical panels are formulated based on Reddy's TSDT coupled with the von Kármán nonlinear strain-displacement relationships. In the modeling, the panel-foundation interaction and thermal effect are also considered. By applying a two-step perturbation approach to solve these equations, the analytical solutions for the two cases of nonlinear vibration and nonlinear bending problems of porous sandwich cylindrical panels are obtained. Numerical comparisons are performed to show the differences between the current model and the EIM.

2 Modeling of porous sandwich cylindrical panels

Consider a porous sandwich cylindrical panel with outer and inner face sheets made of titanium alloy and a core made of aluminum foams reinforced by GPLs. The GPLRC core consists of six layers. Each layer of the porous GPLRC core may have different porosity values and, therefore, the piece-wise FG distribution patterns of porosities across the panel thickness can be achieved. Consider a coordinate system (X, Y, Z) with its origin located at one corner of the panel on the mid-plane, where *X* and *Y* are placed in the axial and circumferential directions, and Z is pointed inward and placed in the panel thickness direction (Figure 1). The panel is of length a in the X direction, length b in the Y direction, the radius of curvature R, and total thickness h. The thickness of the GPLRC core is h_c , while the thickness of each metal face sheet is $h_{\rm f}$. The panel is resting on an elastic foundation that is idealized as a Pasternak-type model with two stiffnesses, where \bar{K}_1 is the vertical spring stiffness and \bar{K}_2 is the shearing layer stiffness.

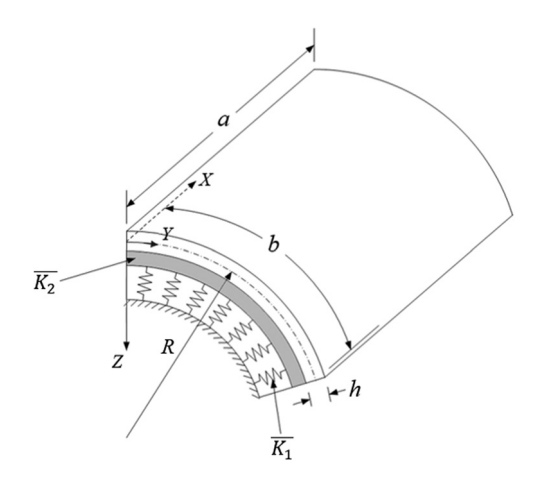


Figure 1: Geometry and the coordinate system of a porous cylindrical panel resting on a Pasternak elastic foundation.

The key issue for analyzing the mechanical response of the GPLRC structures successfully is to determine the material properties of the GPLRC layer accurately and effectively. Since the porous metal foam is slightly anisotropic [33,34], in particular, the shear modulus does not obey the well-known formula of an isotropic material, we introduce an inhomogeneous model instead of the EIM for the porous GPLRC core, where the Young's moduli E_{11} and E_{22} along with the shear modulus G_{12} of the porous GPLRC layer are determined by a generic Halpin-Tsai model [35]:

$$E_{11} = \frac{1 + 2(a_{\text{GPL}}/h_{\text{GPL}})\gamma_{11}^{\text{GPL}}V_{\text{GPL}}}{1 - \gamma_{11}^{\text{GPL}}V_{\text{GPL}}}E^{\text{m}},$$
 (1a)

$$E_{22} = \frac{1 + (2b_{\text{GPL}}/h_{\text{GPL}})y_{22}^{\text{GPL}}V_{\text{GPL}}}{1 - y_{22}^{\text{GPL}}V_{\text{GPL}}}E^{\text{m}},$$
 (1b)

$$G_{12} = \frac{1}{1 - \gamma_{12}^{\text{GPL}} V_{\text{GPL}}} G^{\text{m}},$$
 (1c)

where $a_{\rm GPL}$ is the length, $b_{\rm GPL}$ is the width, and $h_{\rm GPL}$ is the thickness of the GPL; in addition, y_{11}^{GPL} , y_{22}^{GPL} , and y_{12}^{GPL} are defined by

$$\gamma_{11}^{\text{GPL}} = \frac{E_{11}^{\text{GPL}}/E^{\text{m}} - 1}{E_{11}^{\text{GPL}}/E^{\text{m}} + 2a_{\text{GPL}}/h_{\text{GPL}}},$$
 (2a)

$$y_{22}^{\text{GPL}} = \frac{E_{22}^{\text{GPL}}/E^{\text{m}} - 1}{E_{22}^{\text{GPL}}/E^{\text{m}} + 2b_{\text{GPL}}/h_{\text{GPL}}},$$
 (2b)

$$\gamma_{12}^{\text{GPL}} = \frac{G^{\text{GPL}}/G^{\text{m}} - 1}{G^{\text{GPL}}/G^{\text{m}}},$$
 (2c)

in which $E^{\rm GPL}$ and $G^{\rm GPL}$ are the Young's and shear moduli of the GPL, and E^{m} and G^{m} are the Young's and shear moduli of the porous metal matrix.

The mass density and Poisson's ratio of each porous GPLRC layer may be predicted by the rule of the mixture model:

$$\begin{bmatrix} v_{12} \\ \rho \end{bmatrix} = \begin{bmatrix} v^{\text{GPL}} & v^{\text{m}} \\ \rho^{\text{GPL}} & \rho^{\text{m}} \end{bmatrix} \begin{bmatrix} V_{\text{GPL}} \\ V_{\text{m}} \end{bmatrix}, \tag{3}$$

where ρ and ν are the mass density and Poisson's ratio, and $V_{\rm GPL}$ and $V_{\rm m}$ represent the volume fractions of the GPL and metal matrix, respectively.

For a GPLRC layer without porosity, the volume fraction relationship $V_{\rm GPL}$ + $V_{\rm m}$ = 1 is valid, whereas the relationship $V_{GPL} + V_{m} = 1$ is invalid for porous metal foams, as reported in Shen and Li [36]. For this reason, we remove the relationship $V_{GPL} + V_{m} = 1$ for the porous GPLRC layer, and assume that

$$V_{\rm m} + V_{\rm GPL} = 1 - \alpha^*, \tag{4}$$

where α^* represents the porosity coefficient and is given by

$$\alpha^{\star} = 1 - \frac{\rho^{\mathrm{m}}}{\rho^{\mathrm{M}}},\tag{5}$$

with $\rho^{\rm M}$ and $\rho^{\rm m}$ being the mass densities of the metal matrix without or with porosity.

For a porous GPLRC layer, the weight fractions still follow the relationship $w_{GPL} + w_m = 1$. Hence, the relationships between the weight fractions (w_{GPL}, w_m) and the volume fractions (V_{GPL} , V_{m}) for a porous GPLRC layer can be written as

$$w_{\rm GPL} = \frac{V_{\rm GPL}}{V_{\rm GPL} + \frac{\rho^{\rm m}}{\alpha^{\rm GPL}} (1 - \alpha^{\star} - V_{\rm GPL})},$$
 (6a)

$$w_{\rm m} = \frac{V_{\rm m}}{V_{\rm m} + \frac{\rho^{\rm GPL}}{\rho^{\rm m}} (1 - \alpha^{\star} - V_{\rm m})}.$$
 (6b)

In the previous studies [13-24,26-29], the Young's modulus $E^{\rm m}$ of the porous matrix is assumed to obey the Gibson-Ashby model [37], and Poisson's ratio $v^{\rm m}$ is assumed to obey the Roberts-Garboczi model [38]:

$$E^{\rm m} = E^{\rm M}[1 - (\alpha^*)]^2$$
, (7a)

$$v^{\rm m} = 0.221(\alpha^*) + v^{\rm M}[1 - 1.21(\alpha^*) + 0.342(\alpha^*)^2].$$
 (7b)

The main difference between the present model compared with the EIM is that the Young's modulus E^{m} , the shear modulus G^{m} , and Poisson's ratio v^{m} of the porous matrix in equations (1a) and (1b)-(3) are all functions of the porosity coefficient. Mondal et al. [39] reported that the experimental data of the Young's modulus, the shear modulus, and Poisson's ratio for closed-cell porous aluminum foams decreased as the porosity coefficient increased, from which the polynomial fit curves for E^{m} , G^{m} , and ν^{m} are obtained as follows:

$$E^{\rm m} = E^{\rm M}[1.0 - 3.27933(\alpha^*) + 4.68868(\alpha^*)^2 - 3.78983(\alpha^*)^3 + 1.43045(\alpha^*)^4].$$
 (8a)

$$G^{\rm m} = G^{\rm M}[1.0 - 1.34119(\alpha^*) - 1.99118(\alpha^*)^2 + 6.5494(\alpha^*)^3 - 4.55079(\alpha^*)^4],$$
 (8b)

$$v^{\rm m} = v^{\rm M}[1.0 - 0.33684(\alpha^*) + 0.12968(\alpha^*)^2],$$
 (8c)

in which $E^{\rm M}$ is the Young's modulus, $G^{\rm M}$ is the shear modulus, and $\nu^{\rm M}$ is the Poisson's ratio of the matrix without porosity.

The panel is subjected to a transverse dynamic load q (X, Y, \bar{t}) on the outer surface and is located in an elevated temperature environment. The governing equations of motion for porous sandwich cylindrical panels are established based on Reddy's TSDT [40] coupled with the von Kármán nonlinear strain—displacement relationships. These equations can be expressed as

$$\begin{split} \tilde{L}_{11}(\bar{W}) &- \tilde{L}_{12}(\overline{\Psi}_{x}) - \tilde{L}_{13}(\overline{\Psi}_{y}) + \tilde{L}_{14}(\overline{F}) - \tilde{L}_{15}(\bar{N}^{T}) \\ &- \tilde{L}_{16}(\bar{M}^{T}) - \frac{1}{R} \frac{\partial^{2} \bar{F}}{\partial X^{2}} + \bar{K}_{1} \bar{W} - \bar{K}_{2} \nabla^{2} \bar{W} \\ &= \tilde{L}(\bar{W}, \bar{F}) + \tilde{L}_{17}(\ddot{W}) - \left(\tilde{I}_{5} \frac{\partial \ddot{\Psi}_{x}}{\partial X} + \tilde{I}_{5}' \frac{\partial \ddot{\Psi}_{y}}{\partial Y} \right) + q, \end{split}$$
(9a)

$$\tilde{L}_{21}(\bar{F}) + \tilde{L}_{22}(\bar{\Psi}_{x}) + \tilde{L}_{23}(\bar{\Psi}_{y}) - \tilde{L}_{24}(\bar{W}) - \tilde{L}_{25}(\bar{N}^{T})
+ \frac{1}{R} \frac{\partial^{2} \bar{W}}{\partial X^{2}} = -\frac{1}{2} \tilde{L}(\bar{W}, \bar{W}),$$
(9b)

$$\tilde{L}_{31}(\bar{W}) + \tilde{L}_{32}(\bar{\Psi}_{x}) - \tilde{L}_{33}(\bar{\Psi}_{y}) + \tilde{L}_{34}(\bar{F}) - \tilde{L}_{35}(\bar{N}^{T})
- \tilde{L}_{36}(\bar{S}^{T}) = \hat{I}_{5}\frac{\partial \ddot{W}}{\partial y} - \hat{I}_{3}\ddot{\Psi}_{x},$$
(9c)

$$\begin{split} \tilde{L}_{41}(\bar{W}) - \tilde{L}_{42}(\bar{\Psi}_{x}) + \tilde{L}_{43}(\bar{\Psi}_{y}) + \tilde{L}_{44}(\bar{F}) - \tilde{L}_{45}(\bar{N}^{T}) \\ - \tilde{L}_{46}(\bar{S}^{T}) = \hat{I}_{5}' \frac{\partial \ddot{W}}{\partial V} - \hat{I}_{3}' \ddot{\Psi}_{y}, \end{split} \tag{9d}$$

where \bar{W} is the panel displacement in the Z direction; \bar{F} is the stress function defined by $\bar{N}_X = \partial^2 \bar{F}/\partial Y^2$, $\bar{N}_y = \partial^2 \bar{F}/\partial X^2$, and $\bar{N}_{xy} = -\partial^2 \bar{F}/\partial X\partial Y$; and $\bar{\Psi}_X$ and $\bar{\Psi}_Y$ are the rotations of the normal to the middle surface with respect to the Y- and X-axis. $\tilde{L}(\cdot)$ represents the nonlinear operator related to the geometric nonlinearity in the von Kármán sense and can be defined as

$$\tilde{L}(\) = \frac{\partial^2(\)}{\partial X^2} \frac{\partial^2(\)}{\partial Y^2} - 2 \frac{\partial^2(\)}{\partial X \partial Y} \frac{\partial^2(\)}{\partial X \partial Y} + \frac{\partial^2(\)}{\partial Y^2} \frac{\partial^2(\)}{\partial X^2} (10)$$

and other linear operators $\tilde{L}_{ij}()$ in equations (9a)–(9d) are defined in Shen and Xiang [41].

In equation (9a)–(9d), the superposed dots indicate differentiation with respect to time, and the inertias \hat{I}_3 , \hat{I}_5 , etc., are given in detail in equation (23). The panel–foundation interaction, defined by $\bar{K}_1\bar{W}-\bar{K}_2\nabla^2\bar{W}$ and the temperature variation are included, where the thermal forces \bar{N}^T , the thermal moments \bar{M}^T , and the higher-order moments \bar{P}^T caused by elevated temperature are defined by

$$\begin{bmatrix} \bar{N}_{x}^{T} \bar{M}_{x}^{T} \bar{P}_{x}^{T} \\ \bar{N}_{y}^{T} \bar{M}_{y}^{T} \bar{P}_{y}^{T} \\ \bar{N}_{xy}^{T} \bar{M}_{xy}^{T} \bar{P}_{xy}^{T} \end{bmatrix} = \sum_{k=1}^{h_{k}} \int_{h_{k-1}}^{h_{k}} \begin{bmatrix} A_{x} \\ A_{y} \\ A_{xy} \end{bmatrix}_{k} (1, Z, Z^{3}) \Delta T \, dZ, \quad (11a)$$

and \bar{S}^T is defined by

$$\begin{bmatrix} \bar{S}_{x}^{T} \\ \bar{S}_{y}^{T} \\ \bar{S}_{xy}^{T} \end{bmatrix} = \begin{bmatrix} \bar{M}_{x}^{T} \\ \bar{M}_{y}^{T} \\ \bar{M}_{xy}^{T} \end{bmatrix} - \frac{4}{3h^{2}} \begin{bmatrix} \bar{P}_{x}^{T} \\ \bar{P}_{y}^{T} \\ \bar{P}_{xy}^{T} \end{bmatrix}, \tag{11b}$$

where $\Delta T = T - T_0$ is the temperature change from the reference temperature T_0 at which they are free of thermal strains, and

$$\begin{bmatrix} A_{x} \\ A_{y} \\ A_{xy} \end{bmatrix} = - \begin{bmatrix} \bar{Q}_{11} & \bar{Q}_{12} & \bar{Q}_{16} \\ \bar{Q}_{12} & \bar{Q}_{22} & \bar{Q}_{26} \\ \bar{Q}_{16} & \bar{Q}_{26} & \bar{Q}_{66} \end{bmatrix} \begin{bmatrix} 1 & 0 \\ 0 & 1 \\ 0 & 0 \end{bmatrix} \begin{bmatrix} \alpha_{11} \\ \alpha_{22} \end{bmatrix}, \quad (12)$$

in which α_{11} and α_{22} are the thermal expansion coefficients for the *k*th ply, and can be expressed as [42]

$$\alpha_{11} = \frac{V_{\text{GPL}}E^{\text{GPL}}\alpha^{\text{GPL}} + V_{\text{m}}E^{\text{m}}\alpha^{\text{M}}}{V_{\text{GPI}}E^{\text{GPL}} + V_{\text{m}}E^{\text{m}}},$$
 (13a)

$$\alpha_{22} = (1 + \nu^{\text{GPL}}) V_{\text{GPL}} \alpha^{\text{GPL}} + (1 + \nu^{\text{m}}) V_{\text{m}} \alpha^{\text{M}} - \nu_{12} \alpha_{11}$$
 (13b)

in which α^{GPL} and α^{M} are the thermal expansion coefficients of the GPL and metal matrix without porosity. In equation (12), \bar{Q}_{ij} are the transformed elastic constants, as defined in Reddy and Liu [40]. For a porous GPLRC layer, $\bar{Q}_{ij} = Q_{ij}$ in which

$$Q_{11} = \frac{E_{11}}{1 - \nu_{12}\nu_{21}}, \quad Q_{22} = \frac{E_{22}}{1 - \nu_{12}\nu_{21}}, \quad Q_{12} = \frac{\nu_{21}E_{11}}{1 - \nu_{12}\nu_{21}},$$

$$Q_{44} = G_{23},$$

$$Q_{55} = G_{13}, \quad Q_{66} = G_{12}, \quad Q_{16} = Q_{26} = 0,$$

$$(14)$$

where E_{11} , E_{22} , G_{12} , v_{12} , and v_{21} are the Young's and shear moduli and Poisson's ratios for the kth layer.

We assume that the four edges of a porous sandwich cylindrical panel are simply supported without or with in-plane displacements, referred to as 'immovable' or 'movable' edges, respectively. The associated boundary conditions are given by

$$\bar{W} = \bar{\Psi}_{v} = \bar{M}_{v} = \bar{P}_{v} = 0 \text{ (at } X = 0, a),$$
 (15a)

$$\bar{W} = \bar{\Psi}_{Y} = \bar{M}_{V} = \bar{P}_{V} = 0 \text{ (at } Y = 0, b),$$
 (15b)

in which \bar{M}_x and \bar{M}_v are the bending moments and \bar{P}_x and \bar{P}_{ν} are the higher-order moments, as defined in Reddy and Liu [40]. It is noted that, when the temperature increases, \bar{M}_{x} and \bar{M}_{y} contain \bar{M}_{x}^{T} and \bar{M}_{y}^{T} , respectively, and in that case $\bar{M}_x = 0$ and $\bar{M}_y = 0$ become the non-homogeneous boundary conditions.

Meanwhile, the in-plane boundary conditions on the X = (0, a) edges are

$$\bar{U} = 0$$
 (immovable), (16a)

$$\int_{0}^{b} \bar{N}_{x} dY = 0 \quad \text{(movable)}, \tag{16b}$$

and the in-plane boundary conditions on the Y = (0, b)edges are

$$\bar{V} = 0$$
 (immovable), (17a)

$$\int_{0}^{a} \bar{N}_{y} dX = 0 \quad \text{(movable)}, \tag{17b}$$

in which \bar{U} and \bar{V} are the panel displacements in the Xand Y directions.

The immovability conditions of equations (16a) and (17a) may be fulfilled in the average sense as

$$\int_{0}^{b} \int_{0}^{a} \frac{\partial \bar{U}}{\partial X} dX dY = 0, \quad \int_{0}^{a} \int_{0}^{b} \frac{\partial \bar{V}}{\partial Y} dY dX = 0, \quad (18)$$

or

$$\int_{0}^{b} \int_{0}^{a} \left[A_{11}^{\star} \frac{\partial^{2} \bar{F}}{\partial Y^{2}} + A_{12}^{\star} \frac{\partial^{2} \bar{F}}{\partial X^{2}} + \left(B_{11}^{\star} - \frac{4}{3h^{2}} E_{11}^{\star} \right) \frac{\partial \bar{V}_{X}}{\partial X} \right]
+ \left(B_{12}^{\star} - \frac{4}{3h^{2}} E_{12}^{\star} \right) \frac{\partial \bar{V}_{Y}}{\partial Y} - \frac{4}{3h^{2}} \left(E_{11}^{\star} \frac{\partial^{2} \bar{W}}{\partial X^{2}} + E_{12}^{\star} \frac{\partial^{2} \bar{W}}{\partial Y^{2}} \right)$$

$$- \frac{1}{2} \left(\frac{\partial \bar{W}}{\partial X} \right)^{2} - \left(A_{11}^{\star} \bar{N}_{X}^{T} + A_{12}^{\star} \bar{N}_{Y}^{T} \right) \right] dX dY = 0,$$
(19a)

$$\int_{0}^{a} \int_{0}^{b} \left[A_{22}^{\star} \frac{\partial^{2} \bar{F}}{\partial X^{2}} + A_{12}^{\star} \frac{\partial^{2} \bar{F}}{\partial Y^{2}} + \left(B_{21}^{\star} - \frac{4}{3h^{2}} E_{21}^{\star} \right) \frac{\partial \bar{\Psi}_{x}}{\partial X} \right] \\
+ \left(B_{22}^{\star} - \frac{4}{3h^{2}} E_{22}^{\star} \right) \frac{\partial \bar{\Psi}_{y}}{\partial Y} - \frac{4}{3h^{2}} \left(E_{21}^{\star} \frac{\partial^{2} \bar{W}}{\partial X^{2}} + E_{22}^{\star} \frac{\partial^{2} \bar{W}}{\partial Y^{2}} \right)$$

$$+ \frac{\bar{W}}{R} - \frac{1}{2} \left(\frac{\partial \bar{W}}{\partial Y} \right)^{2} - \left(A_{12}^{\star} \bar{N}_{x}^{T} + A_{22}^{\star} \bar{N}_{y}^{T} \right) dY dX = 0.$$
(19b)

In the above equations, the reduced stiffness matrices, such as $[A_{ij}^*]$, $[B_{ij}^*]$, $[D_{ij}^*]$, $[E_{ij}^*]$, $[F_{ij}^*]$, and $[H_{ij}^*]$, are defined as [43]

$$A^* = A^{-1}, B^* = -A^{-1}B, D^* = D - BA^{-1}B,$$

 $E^* = -A^{-1}E, F^* = F - EA^{-1}B, H^* = H - EA^{-1}E,$
(20)

where the panel stiffnesses A_{ii} , B_{ii} ,... are given by

$$(A_{ij}, B_{ij}, D_{ij}, E_{ij}, F_{ij}, H_{ij})$$

$$= \sum_{k=1}^{h_k} \int_{h_{k-1}}^{h_k} (\bar{Q}_{ij})_k (1, Z, Z^2, Z^3, Z^4, Z^6) dZ, \qquad (21a)$$

$$(i, j = 1, 2, 6),$$

$$(A_{ij}, D_{ij}, F_{ij}) = \sum_{k=1}^{n} \int_{h_{k-1}}^{h_k} (\bar{Q}_{ij})_k (1, Z^2, Z^4) dZ,$$
 (21b)

$$(i, j = 4, 5),$$

and the inertias I_i (i = 1, 2, 3, 4, 5, 7) are defined by

$$(I_1, I_2, I_3, I_4, I_5, I_7) = \sum_{k=1}^{n} \int_{h_{k-1}}^{h_k} \rho_k(1, Z, Z^2, Z^3, Z^4, Z^6) dZ, \quad (22)$$

where ρ_k is the mass density of the kth layer, and

$$\bar{I}_{1} = I_{1}, \ \bar{I}_{2} = I_{2} - c_{1}I_{4}, \ \bar{I}_{3} = c_{1}I_{4},
\bar{I}_{4} = \bar{I}_{4}' = I_{3} - 2c_{1}I_{5} + c_{1}^{2}I_{7}, \ \bar{I}_{5} = \bar{I}_{5}' = c_{1}I_{5} - c_{1}^{2}I_{7},
\bar{I}_{1}' = I_{1} + \frac{2}{R}I_{2}, \ \bar{I}_{2}' = I_{2} + \frac{1}{R}I_{3} - c_{1}I_{4} - \frac{c_{1}}{R}I_{5},
\bar{I}_{3}' = c_{1}I_{4} + \frac{c_{1}}{R}I_{5},
\hat{I}_{3} = \bar{I}_{4} - \frac{\bar{I}_{2}\bar{I}_{2}}{\bar{I}_{1}}, \ \hat{I}_{5} = \bar{I}_{5} - \frac{\bar{I}_{2}\bar{I}_{3}}{\bar{I}_{1}}, \ \hat{I}_{7} = \frac{\bar{I}_{3}\bar{I}_{3}}{\bar{I}_{1}} - c_{1}^{2}I_{7},
\hat{I}_{3}' = \bar{I}_{4}' - \frac{\bar{I}_{2}'\bar{I}_{2}'}{\bar{I}_{1}'}, \ \hat{I}_{5}' = \bar{I}_{5}' - \frac{\bar{I}_{2}'\bar{I}_{3}'}{\bar{I}_{1}'}, \ \hat{I}_{7}' = \frac{\bar{I}_{3}'\bar{I}_{3}'}{\bar{I}_{1}'} - c_{1}^{2}I_{7},
\tilde{I}_{5} = \hat{I}_{3} + \hat{I}_{5}, \ \tilde{I}_{5}' = \hat{I}_{3}' + \hat{I}_{5}', \ \tilde{I}_{7} = \hat{I}_{7} - \hat{I}_{5}, \ \tilde{I}_{7}' = \hat{I}_{7}' - \hat{I}_{5}',
\text{ore } c = 4I/(2h^{2})$$

where $c_1 = 4/(3h^2)$.

Solution procedure

A two-step perturbation method was developed in Shen [43]. This approach is successfully employed to solve various nonlinear boundary-value problems of curved panels [44-52]. To apply this two-step perturbation approach to solve nonlinear vibration and nonlinear bending problems of porous sandwich cylindrical panels, the motion equations (9a)-(9d) are first re-written in the non-dimensional forms as

$$\begin{split} L_{11}(W) - L_{12}(\Psi_{x}) - L_{13}(\Psi_{y}) + \gamma_{14} L_{14}(F) - L_{16}(M^{T}) \\ - \eta^{-1} \gamma_{14} \frac{\partial^{2} F}{\partial x^{2}} + K_{1}W - K_{2} \nabla^{2} W \\ = \gamma_{14} \beta^{2} L(W, F) + L_{17}(\ddot{W}) + \left(\gamma_{81} \frac{\partial \ddot{\Psi}_{x}}{\partial x} + \gamma_{82} \beta \frac{\partial \ddot{\Psi}_{y}}{\partial y} \right) + \lambda_{q}, \end{split}$$
(24a)

$$\begin{split} L_{21}(F) + \gamma_{24}L_{22}(\Psi_x) + \gamma_{24}L_{23}(\Psi_y) - \gamma_{24}L_{24}(W) \\ + \eta^{-1}\gamma_{24}\frac{\partial^2 W}{\partial x^2} &= -\frac{1}{2}\gamma_{24}\beta^2 L(W,W), \end{split} \tag{24b}$$

$$\begin{split} L_{31}(W) + L_{32}(\Psi_x) - L_{33}(\Psi_y) + \gamma_{14}L_{34}(F) - L_{36}(S^T) \\ &= \gamma_{83} \frac{\partial \ddot{W}}{\partial x} + \gamma_{91} \ddot{\Psi}_x, \end{split} \tag{24c}$$

$$\begin{split} L_{41}(W) - L_{42}(\Psi_X) + L_{43}(\Psi_Y) + \gamma_{14}L_{44}(F) - L_{46}(S^T) \\ &= \gamma_{84}\beta \frac{\partial \ddot{W}}{\partial \nu} + \gamma_{92} \ddot{\Psi}_{\nu}, \end{split} \tag{24d}$$

where

$$L_{17}(\quad) = \gamma_{170} + \left(\gamma_{171} \frac{\partial^2}{\partial x^2} + \gamma_{172} \beta^2 \frac{\partial^2}{\partial y^2}\right), \tag{25}$$

and the other non-dimensional $L_{ij}(\)$ and $L(\)$ are given in Shen and Xiang [41]. In these equations, the non-dimensional parameters are given by

$$x = \pi \frac{X}{a}, \ y = \pi \frac{Y}{b}, \ \beta = \frac{a}{b}, \ \eta = \frac{\pi^2 R}{a^2} [D_{11}^* D_{22}^* A_{11}^* A_{22}^*]^{1/4},$$

$$W = \frac{\bar{W}}{[D_{11}^* D_{22}^* A_{11}^* A_{22}^*]^{1/4}}, \ F = \frac{\bar{F}}{[D_{11}^* D_{22}^*]^{1/2}},$$

$$(\Psi_x, \Psi_y) = \frac{a}{\pi} \frac{(\bar{\Psi}_x, \bar{\Psi}_y)}{[D_{11}^* D_{22}^* A_{11}^* A_{22}^*]^{1/4}},$$

$$y_{14} = \left[\frac{D_{22}^*}{D_{11}^*}\right]^{1/2}, \ y_{24} = \left[\frac{A_{11}^*}{A_{22}^*}\right]^{1/2}, \ y_5 = -\frac{A_{12}^*}{A_{22}^*},$$

$$(y_{T1}, y_{T2}) = (A_x^T, A_y^T) R \left[\frac{A_{11}^* A_{22}^*}{D_{11}^* D_{22}^*}\right]^{1/4},$$

$$(y_{T4}, y_{T5}, y_{T7}, y_{T8}) = \frac{a^2}{\pi^2 h D_{11}^*} \left[D_x^T, D_y^T, \frac{4}{3h^2} F_x^T, \frac{4}{3h^2} F_y^T\right],$$

$$(M_x, P_x) = \frac{a^2}{\pi^2} \frac{1}{D_{11}^* [D_{11}^* D_{22}^* A_{11}^* A_{22}^*]^{1/4}} \left(\bar{M}_x, \frac{4}{3h^2} \bar{P}_x\right),$$

$$(K_1, k_1) = \bar{K}_1 \left(\frac{a^4}{\pi^4 D_{11}^*}, \frac{b^4}{E_0 h^3}\right),$$

$$(K_2, k_2) = \bar{K}_2 \left(\frac{a^2}{\pi^2 D_{11}^*}, \frac{b^2}{E_0 h^3}\right),$$

$$\omega_L = \Omega_L \frac{a}{\pi} \sqrt{\frac{\rho_0}{E_0}}, \ t = \frac{\pi \bar{t}}{a} \sqrt{\frac{E_0}{\rho_0}}, \ y_{170} = -\frac{I_1 E_0 a^2}{\pi^2 \rho_0 D_{11}^*},$$

$$(y_{91}, y_{92}, y_{81}, y_{82}, y_{83}, y_{84}, y_{171}, y_{172})$$

$$= (-\hat{I}_3, -\hat{I}_3', -\tilde{I}_5, -\tilde{I}_5', \hat{I}_5, \hat{I}_5', -\tilde{I}_7, -\tilde{I}_7') \frac{E_0}{\rho_0 D_{11}^*},$$

in which ρ_0 and E_0 are the reference values of ρ^M and E^M , respectively, for the metal matrix at room temperature; k_1 and k_2 are the non-dimensional forms of foundation stiffnesses used in the numerical examples; and A_x^T , A_y^T , D_x^T ,

 D_v^T , F_x^T , and F_v^T are defined by

$$\begin{bmatrix} A_{x}^{T} & D_{x}^{T} & F_{x}^{T} \\ A_{y}^{T} & D_{y}^{T} & F_{y}^{T} \end{bmatrix} \Delta T = -\sum_{k=1}^{\infty} \int_{h_{k-1}}^{h_{k}} \begin{bmatrix} A_{x} \\ A_{y} \end{bmatrix} (1, Z, Z^{3}) \Delta T dZ. (27)$$

The simply supported boundary conditions of equations (15a) and (15b) can be re-written in non-dimensional forms as

$$W = \Psi_{V} = M_{X} = P_{X} = 0 \text{ (at } X = 0, \pi),$$
 (28a)

$$W = \Psi_x = M_y = P_y = 0$$
 (at $y = 0, \pi$), (28b)

and the in-plane boundary conditions on the $x = (0, \pi)$ edges become

$$\frac{1}{\pi} \int_{0}^{\pi} \beta^2 \frac{\partial^2 F}{\partial y^2} dy = 0 \text{ (movable)}, \tag{29a}$$

$$\int_{0}^{\pi} \int_{0}^{\pi} \left[\left(y_{24}^{2} \beta^{2} \frac{\partial^{2} F}{\partial y^{2}} - y_{5} \frac{\partial^{2} F}{\partial x^{2}} \right) + y_{24} \left(y_{511} \frac{\partial \Psi_{x}}{\partial x} + y_{233} \beta \frac{\partial \Psi_{y}}{\partial y} \right) \right. \\
\left. - y_{24} \left(y_{611} \frac{\partial^{2} W}{\partial x^{2}} + y_{244} \beta^{2} \frac{\partial^{2} W}{\partial y^{2}} \right) - \frac{1}{2} y_{24} \left(\frac{\partial W}{\partial x} \right)^{2} \\
+ \eta^{-1} (y_{24}^{2} y_{T1} - y_{5} y_{T2}) \Delta T \right] dx dy = 0 \text{ (immovable),}$$
(29b)

and the in-plane boundary conditions on the $y = (0, \pi)$ edges become

$$\int_{0}^{\pi} \frac{\partial^{2} F}{\partial x^{2}} dx = 0 \text{ (movable)}, \tag{30a}$$

$$\int_{0}^{\pi} \int_{0}^{\pi} \left[\left(\frac{\partial^{2} F}{\partial x^{2}} - y_{5} \beta^{2} \frac{\partial^{2} F}{\partial y^{2}} \right) + y_{24} \left(y_{220} \frac{\partial \Psi_{x}}{\partial x} + y_{522} \beta \frac{\partial \Psi_{y}}{\partial y} \right) \right]$$

$$- y_{24} \left(y_{240} \frac{\partial^{2} W}{\partial x^{2}} + y_{622} \beta^{2} \frac{\partial^{2} W}{\partial y^{2}} \right) + \eta^{-1} y_{24} W$$

$$- \frac{1}{2} y_{24} \beta^{2} \left(\frac{\partial W}{\partial y} \right)^{2}$$

$$+ \eta^{-1} (y_{T2} - y_{5} y_{T1}) \Delta T dy dx = 0, \text{ (immovable)}.$$

3.1 Nonlinear vibration solutions for porous sandwich cylindrical panels

To explore the nonlinear vibration problem, we need to determine the relationship between the frequency and vibration amplitude of the porous sandwich cylindrical panel. By applying the two-step perturbation approach, the asymptotic solutions of equations (24a)–(24d) satisfying boundary conditions (equations (28a) and (28b)–(30a) and (30b)) are obtained as

$$W(x, y, t) = \varepsilon A_{11}^{(1)}(t) \sin mx \sin ny + (\varepsilon A_{11}^{(1)}(t))^{3} [a_{313} \sin mx \sin 3ny + a_{331} \sin 3mx \sin ny] + O(\varepsilon^{4}),$$
 (31)

 $\Psi_{\chi}(x, y, t)$

$$= [(\varepsilon A_{11}^{(1)}(t))c_{111} + (\varepsilon \ddot{A}_{11}^{(1)}(t))c_{311}] \cos mx \sin ny + (\varepsilon A_{11}^{(1)}(t))^{3}[c_{313} \cos mx \sin 3ny + c_{331} \cos 3mx \sin ny] + O(\varepsilon^{4}),$$
(32)

 $\Psi_{\nu}(x, y, t)$

$$= [(\varepsilon A_{11}^{(1)}(t))d_{111} + (\varepsilon \ddot{A}_{11}^{(1)}(t))d_{311}] \sin mx \cos ny + (\varepsilon A_{11}^{(1)}(t))^{3}[d_{313} \sin mx \cos 3ny + d_{331} \sin 3mx \cos ny] + O(\varepsilon^{4}),$$
(33)

$$F(x, y, t) = -B_{00}^{(0)}y^{2}/2 - b_{00}^{(0)}x^{2}/2 + [(\varepsilon A_{11}^{(1)}(t))b_{111} + (\varepsilon \ddot{A}_{11}^{(1)}(t))b_{311}] \sin mx \sin ny + (\varepsilon A_{11}^{(1)}(t))^{2}[-B_{00}^{(2)}y^{2}/2 - b_{00}^{(2)}x^{2}/2 + b_{220}\cos 2mx + b_{202}\cos 2ny] + (\varepsilon A_{11}^{(1)}(t))^{3}[b_{313}\sin mx \sin 3ny]$$
(34)

+ $b_{331} \sin 3mx \sin ny$] + $O(\varepsilon^4)$,

$$\lambda_{q}(x, y, t) = [(\varepsilon \ddot{A}_{11}^{(1)}(t))g_{30} + (\varepsilon A_{11}^{(1)}(t))g_{31}] \sin mx \sin ny + (\varepsilon A_{11}^{(1)}(t))^{2}[g_{220} \cos 2mx$$

$$+ g_{202} \cos 2ny] + (\varepsilon A_{11}^{(1)}(t))^{3}[g_{33} \sin mx \sin ny] + \dots$$
(35)

It is worth noting that in equations (31)–(35), ε has no specific physical meaning but is definitely a small perturbation parameter in the first step.

For the free vibration problem of the panel, the dynamic load vanishes and we have $\lambda_q = 0$. Employing the Galerkin procedure to equation (35), one has

$$g_{30} \frac{d^{2}(\varepsilon A_{11}^{(1)})}{dt^{2}} + g_{31}(\varepsilon A_{11}^{(1)}) + g_{32}(\varepsilon A_{11}^{(1)})^{2}$$

$$+ g_{33}(\varepsilon A_{11}^{(1)})^{3} = 0.$$
(36)

In the second step, we take $(\varepsilon A_{11}^{(1)})$ as the second perturbation parameter, which relates to the non-dimensional maximum amplitude $W_{\rm max}$. Hence, the solution of equation (36) can be written as

$$\omega_{\rm NL} = \omega_{\rm L} \left[1 + \frac{9g_{31}g_{33} - 10g_{32}^2}{12g_{31}^2} A^2 \right]^{1/2}, \tag{37}$$

where $\omega_{\rm L}=[g_{31}/g_{30}]^{1/2}$ is the non-dimensional linear frequency and $A=W_{\rm max}=\bar{W}_{\rm max}/[D_{11}^*D_{22}^*A_{11}^*A_{22}^*]^{1/4}$ is the non-dimensional amplitude of the panel. In equation (36), g_{30}

to g_{33} are all functions of the porosity coefficient for the porous sandwich cylindrical panel, and details may be found in Appendix A.

3.2 Nonlinear bending solutions for porous sandwich cylindrical panels

For the nonlinear bending problem, we need to determine the relationship between the applied pressure and central deflection of the porous sandwich cylindrical panel. In the present case, the applied pressure is static and uniform and is taken to be $q(x, y, t) = q_0$. Hence, the solutions are independent of time and the terms with respect to the time in equations (24a)–(24d) are vanished. Equation (35) can be re-written as

$$\lambda_q = A_q^{(0)} + A_q^{(1)} (A_{11}^{(1)} \varepsilon) + A_q^{(2)} (A_{11}^{(1)} \varepsilon)^2 + A_q^{(3)} (A_{11}^{(1)} \varepsilon)^3$$
+ ...

in which $(A_{11}^{(1)}\varepsilon)$ is treated as the second perturbation parameter. From equation (31), one has

$$A_{11}^{(1)}\varepsilon = W_{\rm m} + \Theta_3(W_{\rm m})^3 \cdots$$
 (39)

Substituting equation (39) into equation (38), the load–central deflection relationship can be obtained. In equation (38), $A_q^{(j)}$ (j=0-3) are all functions of the porosity coefficient for the porous sandwich cylindrical panel, and details are given in Appendix B.

4 Numerical results and discussion

In this section, the evaluation is made through the free vibration natural frequencies, the nonlinear-to-linear frequency ratio curves, and the nonlinear bending load–deflection curves. The free vibration natural frequencies and the nonlinear-to-linear frequency ratio curves are obtained from equation (37), while the nonlinear bending load–deflection curves are obtained from equations (38) and (39). The reliability and accuracy of the present solution method have been validated by many comparison studies with other research teams using different methods [41,53–55]. In the current research, numerical studies are performed to compare the results obtained from the present model and the EIM, where the equivalent Young's modulus is predicted by a modified Halpin–Tsai model [22].

$$E_{\rm eff} = \frac{3}{8}E_{11} + \frac{5}{8}E_{22},\tag{40}$$

in which E_{11} and E_{22} have the same forms of equation (1a) and (1b), and the shear modulus is expressed by

$$G_{\rm eff} = \frac{E_{\rm eff}}{2(1 + \nu_{\rm eff})},\tag{41}$$

in which

$$v_{\rm eff} = V_{\rm GPL} v^{\rm GPL} + V_m v^m, \tag{42}$$

where $V_{\rm m}=1-V_{\rm GPL}$ and $E^{\rm m}$ and $\nu^{\rm m}$ have the same forms of equations (8a) and (8c). It is noted that in the present model, we use a generic Halpin–Tsai model of equations (1a)–(1c) instead of equation (40), and we remove equation (41) and the relationship $V_{\rm GPL}+V_{\rm m}=1$.

The thermomechanical properties of the metal face sheets and the porous GPLRC core have to be determined first. We select titanium alloy (referred to as Ti–6Al–4V) for the metal face sheets, and the temperature-dependent material properties of Ti–6Al–4V are as follows [25]: $E_{\rm Ti}=122.56\times(1.0-4.586\times10^{-4}T)$ GPa, $\nu_{\rm Ti}=0.29$, $\rho_{\rm Ti}=4,429$ kg/m³, and $\alpha_{\rm Ti}=7.5788\times(1.0+6.638\times10^{-4}T-3.147\times10^{-6}T^2)\times10^{-6}$ /K, where $T=T_0+\Delta T$ and T_0 is set at room temperature.

For the porous GPLRC core, the dimension of the GPL is set as $a_{\rm GPL}=2.5\,\mu{\rm m},\ b_{\rm GPL}=1.5\,\mu{\rm m},\ {\rm and}\ h_{\rm GPL}=1.5\,{\rm nm}.$ Through a literature survey study, we found that the linear fitting formulae $E^{GPL} = (1.112 - 0.00034T)$ TPa, $\alpha^{\rm GPL} = (23.5 + 0.004 \Delta T) \times 10^{-6} / \text{K} [56] \text{ and } E^{\rm GPL} = (1087.8)$ -0.261T) GPa, $\alpha^{GPL} = (13.92 - 0.0299T) \times 10^{-6}$ /K [57] were utilized for GPLs. These equations came from the first author's previous works [58,59] and were only suitable for the monolayer graphene but were invalid for GPLs. Owing to the lack of the experiment data and/or the molecular dynamics (MD) simulation results, the material properties of GPLs are set as follows [60–62]: E^{GPL} = 1,010 GPa, $\rho^{GPL} = 1062.5 \text{ kg/m}^3$, $\nu^{GPL} = 0.186$, and $\alpha^{GPL} = 0.186$ 2.35×10^{-5} /K. The temperature-dependent material properties of the aluminum matrix are set as follows [63]: $E^{\rm M} = 69.0 \times (1.0 - 0.00053\Delta T) \text{ GPa}, v^{\rm M} = 0.29658,$ $\rho^{M} = 2601 \text{ kg/m}^{3}$, and $\alpha^{M} = 23.0 \times (1 + 0.00072\Delta T) \times$ 10^{-6} /°C, where $\Delta T = T - T_0$ and $T_0 = 20$ °C.

In the present study, the GPL weight fraction w_{GPL} is set to be 1–3%. From equations (6a) and (6b), the volume

fractions ($V_{\rm GPL}$, $V_{\rm m}$) of porous GPLRC layers with different porosity coefficient values are obtained and listed in Table 1. The results confirm that the volume fraction relationship must be $V_{\rm GPL}+V_{\rm m}<1$ for the porous GPLRC layers [31].

In the current study, the sandwich cylindrical panel has a total thickness $h=0.05\,\mathrm{m}$, while the thickness of the face sheet is 1 mm. The porous GPLRC core consists of six layers and the thickness of each layer is equal to 8 mm. To conduct a six-layer porous GPLRC core with a piece-wise FG pattern, the porosity coefficient in each layer is selected as $\alpha^{\star}=0.2,\,0.4,\,\mathrm{or}\,0.6.$ Two FG patterns, referred to as FG-X and FG-O, are considered, *i.e.*, the FG-X pattern with $[0.2/0.4/0.6]_\mathrm{S}$ and the FG-O pattern with $[0.6/0.4/0.2]_\mathrm{S}$ (Figure 2). For comparison purposes, a UD pattern core with six layers having an identical porosity coefficient of 0.4 is also considered.

4.1 Vibration characteristics of porous sandwich cylindrical panels

We next focus on the linear and nonlinear vibrations of sandwich cylindrical panels with a porous GPLRC core resting on elastic foundations in thermal environments. The in-plane boundary conditions are set as "immovable." The sandwich panels have a/b = 1, b/h = 20, and a/R = 0.2, 0.5, and 0.8. Typical results are shown in Tables 2–4 and Figures 3–6, in which the non-dimensional frequency is defined by $\tilde{\Omega} = \Omega(b^2/h)\sqrt{\rho_0/E_0}$, where ρ_0 and E_0 are the reference values of $\rho^{\rm M}$ and $E^{\rm M}$, respectively, for the aluminum matrix at $\Delta T = 0$.

Table 2 shows the effects of the weight fraction of GPL and the FG patterns of core porosity on the natural frequency of porous sandwich cylindrical panels with a/R = 0.5 at $\Delta T = 0$. Three GPL weight fractions 1, 2, and 3% are considered. It can be seen that the natural frequencies are increased as the weight fraction $w_{\rm GPL}$ increases. The difference between the two models is about 10% or more, and the maximum difference between the two models is 21.08% for the panel with a porous UD core at $w_{\rm GPL} = 1\%$.

Table 1: Volume fractions of the porous GPLRC layer with different porosity coefficients

W GPL	(V_{GPL}, V_{m})						
	$\alpha^* = 0.2$	$\alpha^* = 0.4$	$\alpha^* = 0.6$	$\alpha^* = 0.8$			
0.01	(0.0155, 0.7845)	(0.0088, 0.5912)	(0.0039, 0.3961)	(0.001, 0.199)			
0.02	(0.0307, 0.7693)	(0.0175, 0.5825)	(0.0078, 0.3922)	(0.002, 0.198)			
0.03	(0.0457, 0.7543)	(0.0261, 0.5739)	(0.0118, 0.3882)	(0.003, 0.197)			

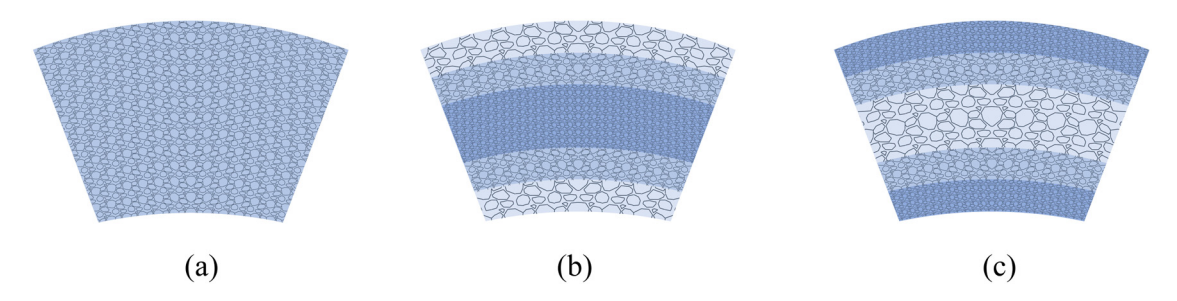


Figure 2: A porous GPLRC core: (a) UD, (b) FG-O, and (c) FG-X.

Table 3 shows the effects of the temperature variation and the FG patterns of core porosity on the natural frequency of porous sandwich cylindrical panels with a/R = 0.8. The GPL weight fraction $w_{\rm GPL} = 3\%$, and the thermal environmental conditions are set as $\Delta T = 0$, 100, and 200 K. Note that the thermal expansion coefficient is taken as $\alpha = \alpha_{11} = \alpha_{22}$ by using the EIM. Like the conventional observation [53], the natural frequencies decrease when the temperature increases. This is due to the fact

that the increase of temperature reduces the panel stiffness which in turn decreases the linear frequencies of the panel. The difference between the two models is about 8% or more, and the maximum difference between the two models is 32.26% for the panel with a porous FG-O core at $\Delta T = 200$ K.

Table 4 shows the effects of the foundation stiffnesses and the FG patterns of core porosity on the natural frequency of porous sandwich cylindrical panels with a/R =

Table 2: Natural frequency $\tilde{\Omega} = \Omega(b^2/h)\sqrt{\rho_0/E_0}$ of porous sandwich cylindrical panels reinforced by GPLs $(h=50 \text{ mm, } a/b=1, b/h=20, a/R=0.5, \Delta T=0)$

W _{GPL}			$ ilde{m{\Omega}}_{11}$	$ ilde{m{\Omega}}_{12}$	$ ilde{arOmega}_{21}$	$ ilde{m{\Omega}}_{22}$	$ ilde{m{\Omega}}_{13}$	$ ilde{m{\Omega}}_{31}$
0.01	UD	Present model	8.2011	15.8791	17.6890	25.5357	30.7112	31.9889
		EIM ^a	6.4727	12.7184	14.1066	20.2790	24.6440	25.6230
		Difference ^b	21.08%	19.90%	20.25%	20.59%	19.76%	19.90%
	FG-O	Present model	7.6483	13.8134	15.9581	22.6151	26.6173	28.1634
		EIM	6.1225	11.2003	12.9311	18.0503	21.8444	23.0738
		Difference	19.95%	18.92%	18.97%	20.18%	17.93%	18.07%
	FG-X	Present model	8.9972	18.1325	19.8045	28.7035	34.9736	36.1468
		EIM	7.4225	15.0236	16.3520	23.6690	28.6817	29.6270
		Difference	17.50%	17.15%	17.43%	17.54%	17.99%	18.04%
0.02	UD	Present model	8.6836	17.0489	19.0376	27.0124	33.2275	34.6933
		EIM	7.2340	14.0798	15.6978	22.4806	27.3054	28.4472
		Difference	16.69%	17.42%	17.54%	16.78%	17.82%	18.00%
	FG-O	Present model	8.0365	14.6577	17.0214	23.6886	28.4762	30.2547
		EIM	6.7926	12.2208	14.2416	19.7256	23.8308	25.2705
		Difference	15.48%	16.63%	16.33%	16.73%	16.31%	16.47%
	FG-X	Present model	9.5731	19.5847	21.3979	30.5573	37.9584	39.2849
		EIM	8.2944	16.7188	18.2450	26.3835	31.9832	33.0676
		Difference	13.36%	14.63%	14.73%	13.66%	15.74%	15.83%
0.03	UD	Present model	9.1050	18.1279	20.2431	28.3839	35.5124	37.1270
		EIM	7.9194	15.3131	17.1339	24.4711	29.7111	30.9968
		Difference	13.02%	15.53%	15.36%	13.79%	16.34%	16.51%
	FG-O	Present model	8.3729	15.4525	17.9767	24.7030	30.2102	32.1753
		EIM	7.4007	13.1625	15.4393	21.2679	25.6619	27.2876
		Difference	11.61%	14.82%	14.11%	13.91%	15.06%	15.19%
	FG-X	Present model	10.0828	20.9029	22.8166	32.2517	40.6130	42.0622
		EIM	9.0760	18.2391	19.9410	28.8130	34.9349	36.1432
		Difference	9.99%	12.74%	12.60%	10.66%	13.98%	14.07%

^aEIM = equivalent isotropic model.

^bDifference = $100\%[\tilde{\Omega}_{ij}(\text{present model}) - \tilde{\Omega}_{ij}(\text{EIM})]/\tilde{\Omega}_{ij}(\text{present model})$.

Table 3: Natural frequency $\tilde{\Omega} = \Omega(b^2/h)\sqrt{\rho_0/E_0}$ of porous sandwich cylindrical panels reinforced by GPLs in thermal environments $(h = 50 \text{ mm}, a/b = 1, b/h = 20, a/R = 0.8, w_{GPL} = 0.03)$

Δ <i>T</i> (K)			$ ilde{m{\Omega}}_{11}$	$ ilde{m{\Omega}}_{12}$	$ ilde{arOmega}_{21}$	$ ilde{arOmega}_{22}$	$ ilde{arOmega}_{13}$	$ ilde{m{\Omega}}_{31}$
0	UD	Present model	11.4800	18.3571	23.3051	29.2218	35.5434	39.4425
		EIM ^a	10.0678	15.5124	19.7960	25.2393	29.7367	32.9255
		Difference ^b	12.30%	15.50%	15.06%	13.63%	16.34%	16.52%
	FG-O	Present model	10.9894	15.7311	21.4879	25.6980	30.2481	34.9283
		EIM	9.8658	13.4173	18.6208	22.2358	25.6946	29.6745
		Difference	10.22%	14.71%	13.34%	13.47%	15.05%	15.04%
	FG-X	Present model	12.3373	21.1087	25.6613	33.0151	40.6411	44.1897
		EIM	11.1753	18.4235	22.4892	29.5329	34.9589	37.9736
		Difference	9.42%	12.72%	12.36%	10.55%	13.98%	14.07%
100	UD	Present model	10.0044	16.3137	21.2590	26.7716	33.2817	36.8454
		EIM	8.6848	13.2599	17.9844	22.9536	27.2794	30.6460
		Difference	13.19%	18.72%	15.40%	14.26%	18.03%	16.83%
	FG-O	Present model	9.2473	12.9703	19.0883	22.6668	27.3175	31.8615
		EIM	8.2881	10.4680	16.4978	19.3914	22.5982	26.9371
		Difference	10.37%	19.29%	13.57%	14.45%	17.28%	15.46%
	FG-X	Present model	10.7738	18.9980	23.5754	30.5029	38.2357	41.5578
		EIM	9.7800	16.2971	20.6841	27.3112	32.5731	35.7134
		Difference	9.22%	14.22%	12.26%	10.46%	14.81%	14.06%
200	UD	Present model	8.2206	13.8587	18.9734	24.0079	30.7349	34.0399
		EIM	7.0334	10.5339	15.9664	20.4111	24.5747	28.1799
		Difference	14.44%	23.99%	15.85%	14.98%	20.04%	17.22%
	FG-O	Present model	7.0132	9.2216	16.2986	19.0527	23.8479	28.4350
		EIM	6.3247	6.2468	14.0533	16.0442	18.9971	23.8822
		Difference	9.82%	32.26%	13.78%	15.79%	20.34%	16.01%
	FG-X	Present model	8.8810	16.5016	21.2537	27.6882	35.5424	38.7218
		EIM	8.1464	13.8440	18.7023	24.8881	29.9938	33.2960
		Difference	8.27%	16.11%	12.00%	10.11%	15.61%	14.01%

^aEIM = equivalent isotropic model.

0.2 at $\Delta T=0$. The GPL weight fraction $w_{\rm GPL}=1\%$. The corresponding foundation stiffnesses are $(k_1, k_2)=(100, 10)$ for the Pasternak foundation, $(k_1, k_2)=(100, 0)$ for the Winkler foundation, and $(k_1, k_2)=(0, 0)$ for the sandwich cylindrical panel without any elastic foundation. Like the conventional observation [53], the natural frequencies are increased as foundation stiffnesses increase. The difference between the two models is about 16% or more, and the maximum difference between the two models is 20.52% for the foundationless panel with a porous UD core.

From Tables 2–4, we observe that the panel with the porous FG-X core has the highest natural frequencies, while the panel with the porous FG-O core has the lowest among the three. Comparing the results obtained from the present model with those obtained from the EIM, it is found that, for most cases, the difference is over 10%, in particular for the case $W_{\text{GPL}} = 1\%$.

For nonlinear vibration analysis, the porous sandwich cylindrical panels have a/R = 0.5 and the GPL weight fraction $w_{\text{GPL}} = 3\%$, except in Figure 4. The effect

of the porosity distribution pattern on the nonlinear-to-linear frequency ratio curves of porous sandwich cylindrical panels at $\Delta T=0$ is shown in Figure 3. Contrary to Tables 2–4, where the panel with the porous FG-X core has the highest natural frequencies, while the panel with the porous FG-O core has the lowest, in Figure 3, the panel with the porous FG-X core has the lowest frequency–amplitude curves, while the panel with the porous FG-O core has the highest among the three. It is observed that the maximum difference between the two models is 2.6% for the panel with the porous FG-O core when the non-dimensional panel deflection \bar{W}/h reaches 1.0. Note that this difference will increase as the panel deflection increases.

DE GRUYTER

Figure 4 shows the effect of the GPL weight fraction on the nonlinear-to-linear frequency ratio curves of sandwich cylindrical panels with the porous FG-X core at $\Delta T = 0$. Three GPL weight fractions $w_{\text{GPL}} = 1$, 2, and 3% are considered. We observe that the frequency–amplitude curve becomes higher when the GPL weight fraction is increased. It can also be seen that the frequency–

^bDifference = 100% $[\tilde{\Omega}_{ii}(\text{present model}) - \tilde{\Omega}_{ii}(\text{EIM})]/\tilde{\Omega}_{ii}(\text{present model})$.

Table 4: Natural frequency $\tilde{\Omega} = \Omega(b^2/h)\sqrt{\rho_0/E_0}$ of porous sandwich cylindrical panels reinforced by GPLs resting on elastic foundations $(h = 50 \text{ mm}, a/b = 1, b/h = 20, a/R = 0.2, w_{GPL} = 0.01, \Delta T = 0)$

(k_1, k_2)			$ ilde{m{\varOmega}}_{11}$	$ ilde{arOmega}_{12}$	$\tilde{\it \Omega}_{21}$	$\tilde{\it \Omega}_{22}$	$ ilde{arOmega}_{13}$	$ ilde{\Omega}_{31}$
(0, 0)	UD	Present model	6.7422	15.7720	16.0868	25.1109	30.6978	30.9303
		EIM ^a	5.3650	12.6362	12.8698	19.9569	24.6335	24.7928
		Difference ^b	20.43%	19.88%	20.00%	20.52%	19.75%	19.84%
	FG-O	Present model	5.9774	13.6839	14.0636	22.1112	26.6010	26.8847
		EIM	4.7734	11.0954	11.3925	17.6428	21.8311	22.0325
		Difference	20.14%	18.92%	18.99%	20.21%	17.93%	18.05%
	FG-X	Present model	7.6313	18.0346	18.3204	28.3112	34.9612	35.1679
		EIM	6.3570	14.9457	15.1672	23.3604	28.6716	28.8250
		Difference	16.70%	17.13%	17.21%	17.95%	17.99%	18.04%
(100, 0)	UD	Present model	16.9385	22.1031	22.3287	29.4760	34.3465	34.5545
		EIM	13.5547	17.7108	17.8782	23.4826	27.5581	27.7006
		Difference	17.85%	19.87%	19.93%	20.33%	19.76%	19.84%
	FG-O	Present model	16.2420	20.3500	20.6072	26.7330	30.5389	30.7864
		EIM	13.3432	16.6588	16.8582	21.5611	25.0940	25.2694
		Difference	17.85%	18.14%	18.19%	19.35%	17.83%	17.92%
	FG-X	Present model	16.9045	23.4719	23.6922	32.0252	38.0189	38.2091
		EIM	13.9814	19.4282	19.5991	26.4384	31.2232	31.3641
		Difference	17.29%	17.23%	17.28%	17.45%	17.87%	17.91%
(100, 10)	UD	Present model	27.6321	40.8883	41.0108	52.4422	59.3463	59.4671
		EIM	22.1265	32.7663	32.8571	41.9605	47.6020	47.6846
		Difference	19.92%	19.86%	19.88%	19.99%	19.79%	19.81%
	FG-O	Present model	26.7209	39.1624	39.2967	49.9709	56.1555	56.2906
		EIM	22.0114	32.2411	32.3446	40.9605	46.2691	46.3645
		Difference	17.62%	17.67%	17.69%	18.03%	17.61%	17.63%
	FG-X	Present model	27.1087	40.7999	40.9271	52.8673	60.3975	60.5175
		EIM	22.3958	33.7316	33.8303	43.6948	49.8321	49.9205
		Difference	17.39%	17.32%	17.34%	17.35%	17.49%	17.51%

^aEIM = equivalent isotropic model.

^bDifference = 100% $[\tilde{\Omega}_{ii}(\text{present model}) - \tilde{\Omega}_{ii}(\text{EIM})]/\tilde{\Omega}_{ij}(\text{present model})$.

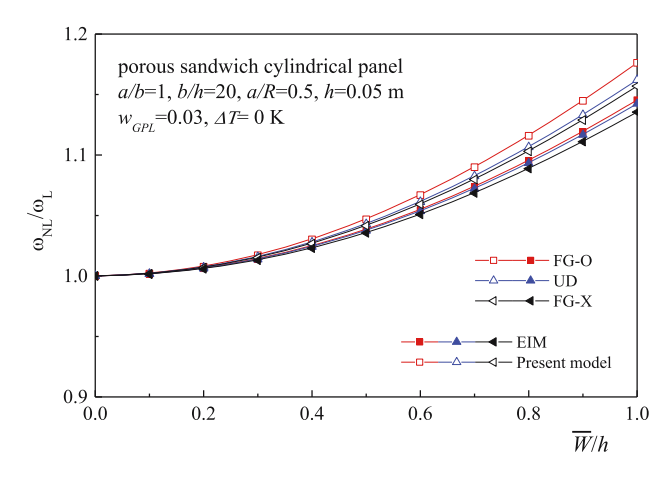


Figure 3: Effect of the porosity distribution pattern on the frequency—amplitude curves of porous sandwich cylindrical panels reinforced by GPLs.

amplitude curves with $w_{GPL} = 2$ and 3% obtained from the present model are higher than those obtained based on the EIM, while for the case of $w_{GPL} = 1\%$, the results

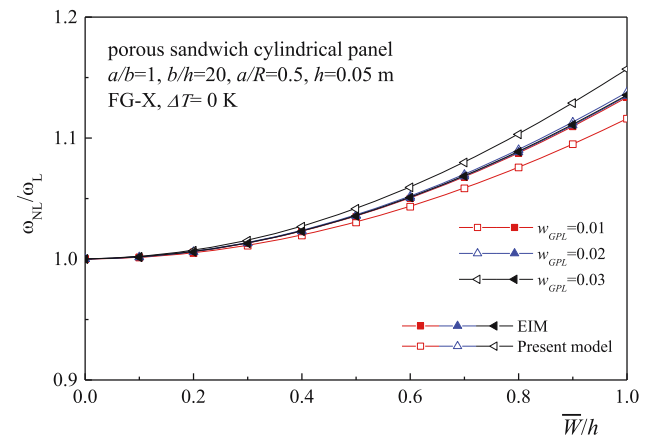


Figure 4: Effect of the GPL weight fraction on the frequency-amplitude curves of porous sandwich cylindrical panels reinforced by GPLs.

are inversed. In this example, the maximum difference between the two models is only 1.9% for the porous panel with $w_{\rm GPL} = 3\%$ when \bar{W}/h reaches 1.0.

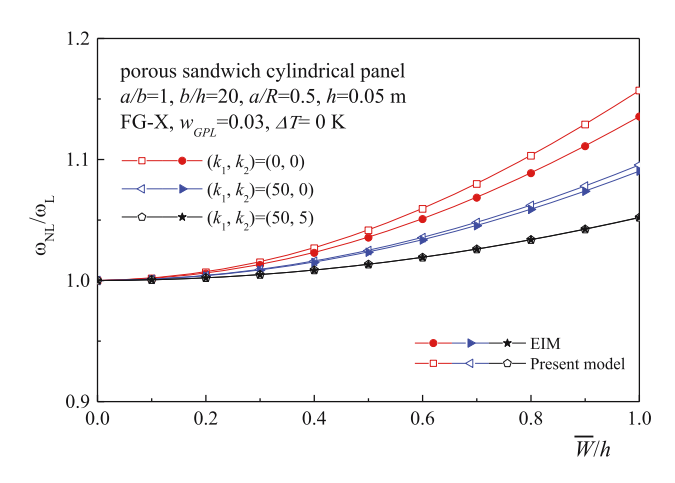


Figure 5: Effect of foundation stiffnesses on the frequency-amplitude curves of porous sandwich cylindrical panels reinforced by GPLs resting on elastic foundations.

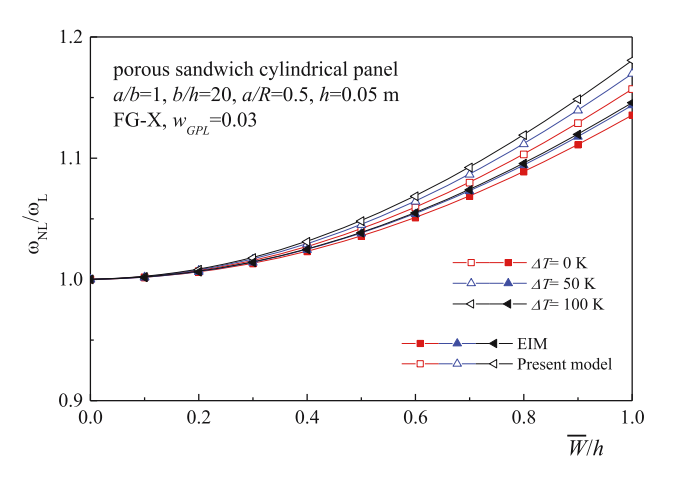


Figure 6: Effect of temperature variation on the frequency—amplitude curves of porous sandwich cylindrical panels reinforced by GPLs in thermal environments.

Figure 5 shows the effect of foundation stiffnesses on the nonlinear-to-linear frequency ratio curves of sandwich cylindrical panels with the porous FG-X core resting on elastic foundations at $\Delta T=0$. Two foundation models are considered where $(k_1, k_2)=(50, 5)$ for the Pasternak foundation and $(k_1, k_2)=(50, 0)$ for the Winkler foundation. Contrary to the results in Table 4, where the natural frequencies are increased with an increase in foundation stiffnesses, in Figure 5, the frequency–amplitude curves are reduced with an increase in foundation stiffnesses. In this example, the maximum difference between the two models is only 1.9% for the foundationless panel when \bar{W}/h reaches 1.0, and the difference may be neglected when the panel rests on a Pasternak foundation with $(k_1, k_2)=(50, 5)$.

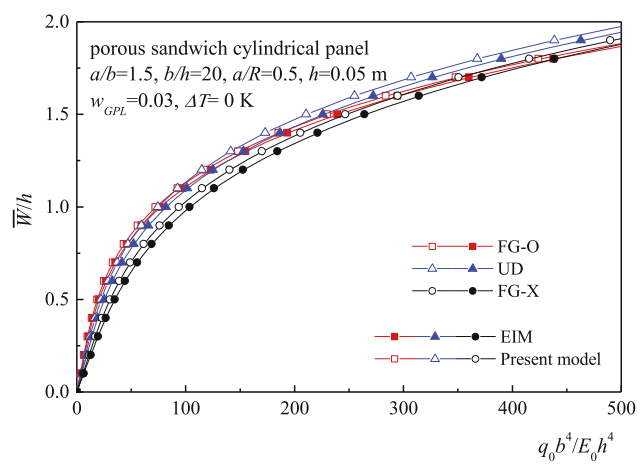


Figure 7: Effect of porosity distribution pattern on the nonlinear bending load-deflection curves of porous sandwich cylindrical panels reinforced by GPLs.

Figure 6 shows the effect of temperature variation on the nonlinear-to-linear frequency ratio curves of sandwich cylindrical panels with the porous FG-X core in thermal environments. The thermal environmental conditions are taken as $\Delta T=0$, 50, and 100 K. Contrary to the results in Table 3, where the natural frequencies are decreased with an increase in the temperature, in Figure 6, the frequency–amplitude curves are increased with an increase in the temperature. In this example, we observe that the maximum difference between the two models is 3% for the porous panel at $\Delta T=100$ K when \bar{W}/h reaches 1.0.

4.2 Nonlinear bending responses of porous sandwich cylindrical panels

Then, we turn our attention to the nonlinear bending of sandwich cylindrical panels with the porous GPLRC core resting on elastic foundations in thermal environments. The sandwich panels have a/b = 1.5, b/h = 20, and a/R = 0.5. The GPL weight fraction $w_{\text{GPL}} = 3\%$, except in Figure 8.

Figure 7 shows the effect of the porosity distribution pattern on the nonlinear bending load–deflection curves of porous sandwich cylindrical panels at $\Delta T=0$. Like the conventional observation [54], the panel with the porous FG-X core has the lowest nonlinear bending load–deflection curves, while the panel with the porous FG-O core has the highest among the three when the non-dimensional panel deflection $\bar{W}/h \leq 1.0$. Unlike the conventional observation [54], the bending load–deflection curve of the panel with porous UD core becomes the highest among the three when the panel deflection $\bar{W}/h > 1.0$. In this example, we observe

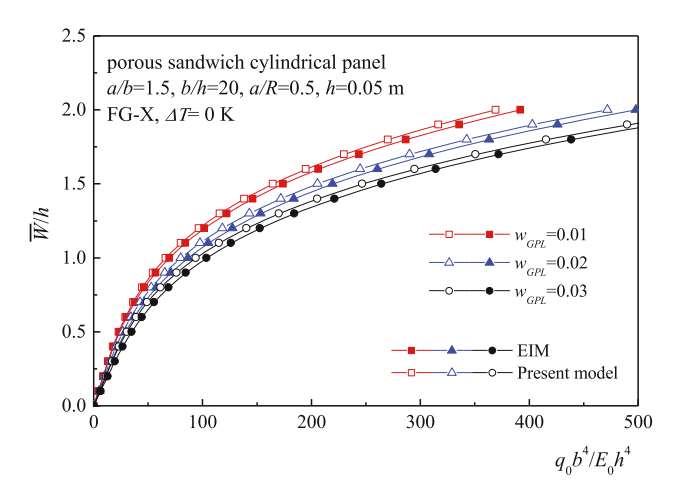


Figure 8: Effect of the GPL weight fraction on the nonlinear bending load-deflection curves of porous sandwich cylindrical panels reinforced by GPLs.

that the maximum difference between the two models is 5.1% for the panel with the porous UD core when \bar{W}/h reaches 2.0.

Figure 8 shows the effect of the GPL weight fraction on the nonlinear bending load–deflection curves of sandwich cylindrical panels with the porous FG-X core at $\Delta T=0$. Three GPL weight fractions 1, 2, and 3% are considered. It is observed that the nonlinear bending load–deflection curves are reduced with an increase in the GPL weight fraction. In this example, we observe that the maximum difference between the two models is 6.1% for the panel with $w_{\rm GPL}=1\%$ when \bar{W}/h reaches 2.0.

Figure 9 shows the effect of foundation stiffnesses on the nonlinear bending load–deflection curves of sandwich

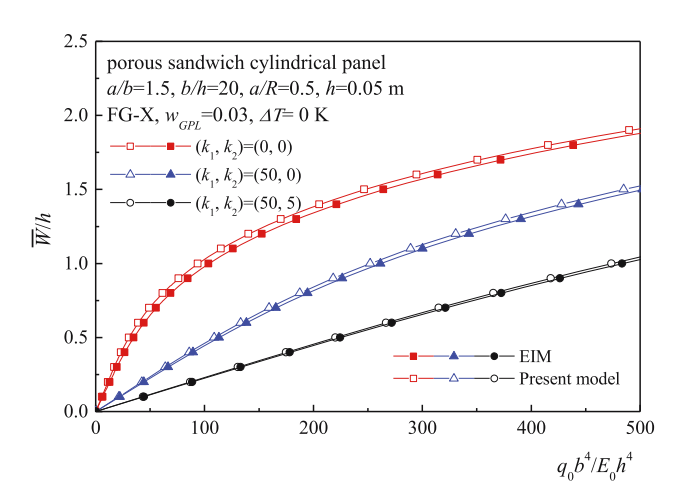


Figure 9: Effect of foundation stiffnesses on the nonlinear bending load-deflection curves of porous sandwich cylindrical panels reinforced by GPLs resting on elastic foundations.

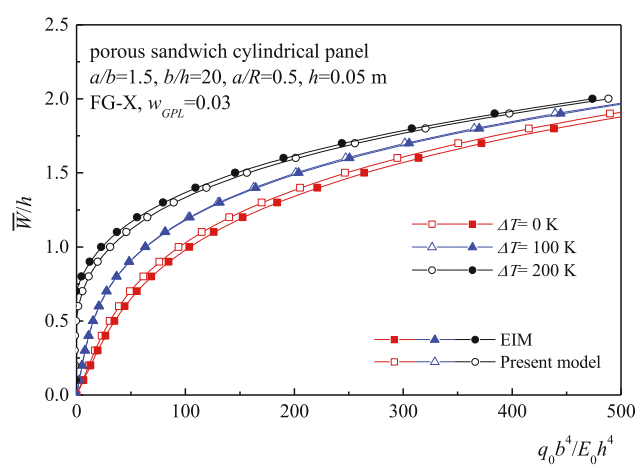


Figure 10: Effect of temperature variation on the nonlinear bending load-deflection curves of porous sandwich cylindrical panels reinforced by GPLs in thermal environments.

cylindrical panels with the porous FG-X core resting on elastic foundations at $\Delta T=0$. The same two foundation models are adopted as in Figure 5. It is observed that the nonlinear bending load–deflection curves are reduced as the foundation stiffnesses increase. In this example, we observe that the maximum difference between the two models is 4.7% for the foundationless panel when \bar{W}/h reaches 2.0. The difference between the two models may be neglected when the foundation stiffness is sufficiently large.

Figure 10 shows the effect of temperature variation on the nonlinear bending load–deflection curves of sandwich cylindrical panels with the porous FG-X core in thermal environments. The thermal environmental conditions are set as $\Delta T=0$, 100, and 200 K. Like the conventional observation [54], the nonlinear bending load–deflection curve becomes higher when the temperature increases. Unlike the conventional observation [54], the small initial deflection can be observed at $\Delta T=100$ and 200 K. In this example, we observe that the maximum difference between the two models is 4.7% for the panel at $\Delta T=0$ when \bar{W}/h reaches 2.0.

5 Conclusions

The quantitative evaluation for the nonlinear vibration and nonlinear bending of sandwich cylindrical panels with the porous metal core reinforced by GPLs has been presented. The FG material concept is incorporated into the design of the porous GPLRC layer. By introducing an inhomogeneous model, the Young's moduli along with

the shear modulus for the porous GPLRC layer are predicted through a generic Halpin-Tsai model containing a porosity coefficient. Comparison investigations between the present model and the EIM have been presented for the sandwich cylindrical panels with the porous UD, FG-O, or FG-X GPLRC core. The numerical results reveal that, in most cases, the natural frequencies, the frequencyamplitude curves, and the bending load-deflection curves of the porous sandwich cylindrical panels are underestimated by using the EIM. In contrast, for some special cases, the frequency-amplitude curves of sandwich cylindrical panels with the porous FG-X core under $w_{GPL} = 1\%$ at $\Delta T = 0 \text{ K}$, and/or the bending load-deflection curves of the sandwich cylindrical panels with the porous FG-X core under $w_{GPL} = 3\%$ at $\Delta T = 200$ K are overestimated by using the EIM. In most cases, the difference between the two models is over 10% for the natural frequencies and the maximum difference between the two models may reach 32.26%. The difference between the two models is relatively small for the frequency-amplitude curves and the bending load-deflection curves of the sandwich cylindrical panels with the porous GPLRC core. Only in the case when the panel rests on a Pasternak elastic foundation with sufficiently large foundation stiffnesses, the difference between the two models may be negligible, and the EIM may be valid.

Funding information: The authors state that no funding was involved.

Author contributions: All authors have accepted responsibility for the entire content of this manuscript and approved its submission.

Conflict of interest: The authors state that there is no conflict of interest.

References

- Lu G, Lu GQ, Xiao ZM. Mechanical properties of porous materials. J Porous Mater. 1999;6:359–68.
- [2] Banhart J. Manufacture, characterisation and application of cellular metals and metal foams. Prog Mater Sci. 2001;46:559-632.
- [3] Lefebvre L-P, Banhart J, Dunand D. Porous metals and metallic foams: Current status and recent developments. Adv Eng Mater. 2008;10:775–87.
- [4] Babaei1 M, Kiarasi1 F, Asemi K, Hosseini M. Functionally graded saturated porous structures: A review. J Comput Appl Mech. 2022;53:297–308.

- [5] Kalpakoglou T, Yiatros S. Metal foams: A review for mechanical properties under tensile and shear stress. Front Mater. 2022;9:998673.
- [6] Kiarasi1 F, Babaei1 M, Asemi K, Dimitri R, Tornabene F. Threedimensional buckling analysis of functionally graded saturated porous rectangular plates under combined loading conditions. Appl Sci. 2021;11:10434.
- [7] Babaei1 M, Hajmohammad MH, Asemi K. Natural frequency and dynamic analyses of functionally graded saturated porous annular sector plate and cylindrical panel based on 3D elasticity. Aerosp Sci Technol. 2020;96:105524.
- [8] Babaei1 M, Asemi K, Kiarasi1 F. Static response and freevibration analysis of a functionally graded annular elliptical sector plate made of saturated porous material based on 3D finite element method. Mech Based Des Struct Mach. 2023:51:1272-96.
- [9] Barbaros I, Yang Y, Safaei B, Yang Z, Qin Z, Asmael M. State-ofthe-art review of fabrication, application, and mechanical properties of functionally graded porous nanocomposite materials. Nanotechnol Rev. 2022;11:321–71.
- [10] You X, Zhang Q, Yang J, Dong S. Review on 3D-printed graphene-reinforced composites for structural applications. Compos Part A-Appl Sci Manufact. 2023;167:107420.
- [11] Duarte I, Ventura E, Olhero S, Ferreira JM. An effective approach to reinforced closed-cell Al-alloy foams with multiwalled carbon nanotubes. Carbon. 2015;95:589-600.
- [12] Li M, Gao H, Liang J, Gu S, You W, Shu D, et al. Microstructure evolution and properties of graphene nanoplatelets reinforced aluminum matrix composites. Mater Character. 2018;140:172-8.
- [13] Li K, Wu D, Chen X, Cheng J, Liu Z, Gao W, et al. Isogeometric analysis of functionally graded porous plates reinforced by graphene platelets. Compos Struct. 2018;204:114–30.
- [14] Phan DH. Isogeometric analysis of functionally-graded graphene platelets reinforced porous nanocomposite plates using a refined plate theory. Int J Struct Stabil Dyn. 2020;20:2050076.
- [15] Nguyen NV, Nguyen-Xuan H, Lee D, Lee J. A novel computational approach to functionally graded porous plates with graphene platelets reinforcement. Thin-Walled Struct. 2020:150:106684.
- [16] Nguyen NV, Nguyen-Xuan H, Lee J. A quasi-three-dimensional isogeometric model for porous sandwich functionally graded plates reinforced with graphene nanoplatelets. J Sandw Struct Mater. 2022;24:825–59.
- [17] Fan X, Wang A, Jiang P, Wu S, Sun Y. Nonlinear bending of sandwich plates with graphene nanoplatelets reinforced porous composite core under various loads and boundary conditions. Mathematics. 2022;10:3396.
- [18] Gao K, Gao W, Chen D, Yang J. Nonlinear free vibration of functionally graded graphene platelets reinforced porous nanocomposite plates resting on elastic foundation. Compos Struct. 2018;204:831–46.
- [19] Pan H-G, Wu Y-S, Zhou J-N, Fu Y-M, Liang X, Zhao T-Y. Free vibration analysis of a graphene-reinforced porous composite plate with different boundary conditions. Materials. 2021:14:3879.
- [20] Teng MW, Wang YQ. Nonlinear forced vibration of simply supported functionally graded porous nanocomposite thin

- plates reinforced with graphene platelets. Thin-Walled Struct. 2021;164:107799.
- [21] Huang X, Wang C, Wang J, Wei N. Nonlinear vibration analysis of functionally graded porous plates reinforced by graphene platelets on nonlinear elastic foundations. Strojniski Vestnik-J Mech Eng. 2022;68:571-82.
- [22] Yang J, Chen D, Kitipornchai S. Buckling and free vibration analyses of functionally graded graphene reinforced porous nanocomposite plates based on Chebyshev-Ritz method. Compos Struct. 2018;193:281-94.
- [23] Saidia AR, Bahaadinia R, Majidi-Mozafari K. On vibration and stability analysis of porous plates reinforced by graphene platelets under aerodynamical loading. Compos Part B- Eng. 2019:164:778-99.
- [24] Safarpour M, Rahimi A, Alibeigloo A, Bisheh H, Forooghi A. Parametric study of three-dimensional bending and frequency of FG-GPLRC porous circular and annular plates on different boundary conditions. Mech Based Des Struct Mach. 2021:49:707-37.
- [25] Shen H-S. Functionally graded materials nonlinear analysis of plates and shells. Boca Raton: CRC Press; 2009.
- [26] Zhou X, Wang Y, Zhang W. Vibration and flutter characteristics of GPL-reinforced functionally graded porous cylindrical panels subjected to supersonic flow. Acta Astron. 2021;183:89-100.
- [27] Twinkle CM, Pitchaimani J. Free vibration and stability of graphene platelet reinforced porous nano-composite cylindrical panel: Influence of grading, porosity and non-uniform edge loads. Eng Struct. 2021;230:111670.
- [28] Twinkle CM, Pitchaimani J. Static stability and vibration behavior of graphene platelets reinforced porous sandwich cylindrical panel under non-uniform edge loads using semianalytical approach. Compos Struct. 2022;280:114837.
- [29] Sun X, Chi W, Luo J. Free vibration analysis of a grapheneplatelet-reinforced, porous, two-cylindrical-panel system. Materials. 2022;15:6158.
- [30] Moradi-Dastjerdi R, Radhi A, Behdinan K. Damped dynamic behavior of an advanced piezoelectric sandwich plate. Compos Struct. 2020;243:112243.
- [31] Shen H-S, Li C. Modeling and re-examination of nonlinear vibration and nonlinear bending of sandwich plates with porous FG-GPLRC core. Adv Eng Mater. 2023. doi: 10.1002/ adem.202300299.
- [32] Chen XH, Shen H-S, Xiang Y. Re-examination of thermomechanical buckling and postbuckling responses of sandwich plates with porous FG-GPLRC core. Thin-Walled Struct. 2023;187:110735.
- [33] Simone AE, Gibson LJ. Effects of solid distribution on the stiffness and strength of metallic foams. Acta Mater. 1998;46:2139-50.
- [34] Roberts AP, Garboczi EJ. Elastic moduli of model random three dimensional closed-cell cellular solids. Acta Mater. 2001:49:189-97.
- [35] Halpin JC, Kardos JL. The Halpin-Tsai equations: A review. Polym Eng Sci. 1976;16:344-52.
- [36] Shen H-S, Li C. Modeling and evaluation for large amplitude vibration and nonlinear bending of perovskite solar cell. Compos Struct. 2023;303:116235.
- [37] Gibson LJ, Ashby MF. The mechanics of three-dimensional cellular materials. Proc R Soc Lond A. 1982;382:43-59.

- [38] Roberts A, Garboczi EJ. Computation of the linear elastic properties of random porous materials with a wide variety of microstructure. Proc R Soc Lond A. 2002;458:1033-54.
- [39] Mondal DP, Ramakrishnan N, Suresh KS, Das S. On the moduli of closed-cell aluminum foam. Scr Mater. 2007;57:929-32.
- [40] Reddy JN, Liu CF. A higher-order shear deformation theory of laminated elastic shells. Int J Eng Sci. 1985;23:319-30.
- [41] Shen H-S, Xiang Y. Nonlinear vibration of nanotube-reinforced composite cylindrical panels resting on elastic foundations in thermal environments. Compos Struct. 2014;111:291-300.
- [42] Schapery RA. Thermal expansion coefficients of composite materials based on energy principles. J Compos Mater. 1968;2:380-404.
- [43] Shen H-S. A two-step perturbation method in nonlinear analysis of beams, plates and shells. Germany: John Wiley & Sons Inc; 2013.
- [44] Li Z-M, Zhao Y-X, Chen X-D. Non-linear buckling and postbuckling behavior of 3d braided cylindrical panels under axial compression in thermal environments. Mech Adv Mater Struct. 2014;21:490-504.
- [45] Sahmani S, Fattahi AM. Imperfection sensitivity of the sizedependent nonlinear instability of axially loaded FGM nanopanels in thermal environments. Acta Mech. 2017;228:3789-810.
- [46] Zhao Y-X, Liu T, Li Z-M. Nonlinear bending analysis of a 3D braided composite cylindrical panel subjected to transverse loads in thermal environments. Chin J Aeron. 2018;31:1716-27.
- Bayat MR, Mashhadi MM. Low-velocity impact response of [47] sandwich cylindrical panels with nanotube-reinforced and metal face sheet in thermal environment. Aeronaut J. 2018;122:1943-66.
- [48] Babaei H, Kiani Y, Eslami MR. Application of two-steps perturbation technique to geometrically nonlinear analysis of long FGM cylindrical panels on elastic foundation under thermal load. J Therm Stress. 2018;41:847-65.
- [49] Babaei H, Kiani Y, Eslami MR. Large amplitude free vibrations of long FGM cylindrical panels on nonlinear elastic foundation based on physical neutral surface. Compos Struct. 2019;220:888-98.
- [50] Ma W, Yang C, Ma D, Zhong JL. Low-velocity impact response of nanotube-reinforced composite sandwich curved panels. SADHANA-Acad Proc Eng Sci. 2019;44:227.
- [51] Babaei H, Eslami MR. Nonlinear analysis of thermal-mechanical coupling bending of FGP infinite length cylindrical panels based on PNS and NSGT. Appl Math Model. 2021;91:1061-80.
- [52] Babaei H. Thermomechanical analysis of snap-buckling phenomenon in long FG-CNTRC cylindrical panels resting on nonlinear elastic foundation. Compos Struct. 2022;286:115199.
- Shen H-S, Xiang Y, Fan Y, Hui D. Nonlinear vibration of functionally graded graphene-reinforced composite laminated cylindrical panels resting on elastic foundations in thermal environments. Compos Part B-Eng. 2018;136:177-86.
- Shen H-S, Xiang Y, Fan Y, Hui D. Nonlinear bending analysis of FG-GRC laminated cylindrical panels on elastic foundations in thermal environments. Compos Part B-Eng. 2018;141:148-57.
- [55] Shen H-S, Xiang Y, Fan Y. Large amplitude vibration of doubly curved FG-GRC laminated panels in thermal environments. Nanotechnol Rev. 2019;8:467-83.
- [56] Li X, Chen XC, Jiang WT. Dynamic stability of graded graphene reinforced truncated conical shells under both periodic

- spinning speeds and axial loads considering thermal effects. Eng Struct. 2022;256:113963.
- [57] Xu Z, Huang Q. Vibro-acoustic analysis of functionally graded graphene-reinforced nanocomposite laminated plates under thermal-mechanical loads. Eng Struct. 2019;186:345–55.
- [58] Lin F, Xiang Y, Shen H-S. Temperature dependent mechanical properties of graphene reinforced polymer nanocomposites – A molecular dynamics simulation. Compos B-Eng. 2017;111:261–9.
- [59] Shen H-S, Xiang Y, Lin F. Nonlinear vibration of functionally graded graphene- reinforced composite laminated plates in thermal environments. Comput Methods Appl Mech Eng. 2017;319:175-93.
- [60] Rafiee MA, Rafiee J, Wang Z, Song H, Yu Z-Z, Koratkar N. Enhanced mechanical properties of nanocomposites at low graphene content. ACS Nano. 2009;3:3884-90.
- [61] Liu F, Ming P, Li J. Ab initio calculation of ideal strength and phonon instability of graphene under tension. Phys Rev B. 2007;76:064120.
- [62] Wu H, Drzal LT. Effect of graphene nanoplatelets on coefficient of thermal expansion of polyetherimide composite. Mater Chem Phys. 2014;146:26–36.
- [63] Shen H-S, Wang H. Thermal postbuckling of functionally graded fiber reinforced composite cylindrical shells surrounded by an elastic medium. Compos Struct. 2013;102:250-60.

Appendix

Appendix A

In equation (36).

$$\begin{split} g_{30} &= -[\gamma_{170} - (\gamma_{171}m^2 + \gamma_{172}n^2\beta^2)] \\ &- \frac{\gamma_{81}m^2g_{04} + \gamma_{82}n^2\beta^2g_{03}}{g_{00}} \\ &+ \gamma_{14}\gamma_{24}\frac{g_{05}^*}{g_{06}}\frac{\gamma_{81}m^2g_{02} + \gamma_{82}n^2\beta^2g_{01}}{g_{00}} - g_{08}^* \\ &- \gamma_{14}\gamma_{24}\frac{g_{07}^*g_{05}^{**}}{g_{06}}, \\ g_{31} &= Q_{11} - D_{02}, \ g_{33} &= \frac{1}{16}\gamma_{14}\gamma_{24}\left(\frac{m^4}{\gamma_7} + \frac{n^4\beta^4}{\gamma_6}\right) - D_{22}, \\ g_{32} &= -\frac{2}{3\pi^2mn}\gamma_{14}\gamma_{24}m^2n^2\beta^2\left(\frac{\gamma_8}{\gamma_6} + \frac{\gamma_9}{\gamma_7} + \frac{1}{4m^2\eta\gamma_6}\right) \\ &+ 4\frac{g_{05}^*}{g_{06}}\right)(1 - \cos m\pi)(1 - \cos n\pi), \\ &+ 2g_{33}\Phi(T) \end{split}$$

in the above equations (other symbols are defined as in ref. [41])

$$Q_{11} = g_{08} + \gamma_{14} \gamma_{24} \frac{g_{05}^{*} g_{07}^{*}}{g_{06}} + [K_{1} + K_{2}(m^{2} + n^{2}\beta^{2})],$$

$$D_{02} = \gamma_{14} (B_{000}m^{2} + b_{000}n^{2}\beta^{2}),$$

$$D_{22} = \gamma_{14} (B_{200}m^{2} + b_{200}n^{2}\beta^{2}),$$
(A.2)

and

$$\Phi(T) = \lambda + \Theta_2(\lambda)^2 + \Theta_3(\lambda)^3 + \cdots, \tag{A.3}$$

where (with m = n = 1)

$$\begin{split} \lambda &= \frac{16}{\pi^2 G_{08}} \Biggl((\gamma_{T4} m^2 + \gamma_{T5} n^2 \beta^2) \\ &- \frac{(\gamma_{T4} - \gamma_{T7}) m^2 g_{102} + (\gamma_{T5} - \gamma_{T8}) n^2 \beta^2 g_{101}}{g_{00}} \Biggr) \Delta T \\ &\times \frac{h}{[D_{11}^* D_{22}^* A_{11}^* A_{22}^*]^{1/4}}, \\ \Theta_2 &= \frac{8}{3\pi^2 G_{08}} \gamma_{14} \gamma_{24} m^2 n^2 \beta^2 \Biggl(\frac{\gamma_8}{\gamma_6} + \frac{\gamma_9}{\gamma_7} + \frac{1}{4 m^2 \eta \gamma_6} \Biggr) \\ &+ 4 \frac{g_{05}^*}{g_{06}} \Biggr), \\ \Theta_3 &= 2\Theta_2^2 - \frac{g_{33}}{G_{08}}, \ G_{08} = Q_{11} - D_{02}, \end{split}$$

and for the case of "movable" edges,

$$B_{000} = B_{200} = b_{000} = b_{200} = 0,$$
 (A.5)

and for the case of "immovable" edges,

$$B_{000} = \eta^{-1} \gamma_{T1} \Delta T, \ B_{200} = -\frac{1}{8} \gamma_{24} \frac{m^2 + \gamma_5 n^2 \beta^2}{\gamma_{24}^2 - \gamma_5^2},$$

$$b_{000} = \eta^{-1} \gamma_{T2} \Delta T, \ b_{200} = -\frac{1}{8} \gamma_{24} \frac{\gamma_5 m^2 + \gamma_{24}^2 n^2 \beta^2}{\gamma_{24}^2 - \gamma_5^2}$$
(A.6)

Appendix B

In equations (38) and (39).

$$A_{q}^{(0)} = -\left(\frac{1}{mn}(\gamma_{T4}m^{2} + \gamma_{T5}n^{2}\beta^{2}) - \gamma_{14}\gamma_{24}\frac{g_{07}^{*}g_{01}^{*}}{g_{06}}\right)$$

$$-g_{02}^{*}\frac{16}{n^{2}}\Delta T\frac{h}{[D_{11}^{*}D_{22}^{*}A_{11}^{*}A_{22}^{*}]^{1/4}},$$

$$A_{q}^{(1)} = C_{11}G_{08}, A_{q}^{(2)} = -C_{11}\left[\frac{8}{3\pi^{2}}\gamma_{14}\gamma_{24}m^{2}n^{2}\beta^{2}\left(\frac{\gamma_{8}}{\gamma_{6}} + \frac{\gamma_{9}}{\gamma_{7}}\right)\right]$$

$$+4\frac{g_{05}^{*}}{g_{06}} + \frac{1}{4m^{2}\gamma_{6}\eta}\right],$$

$$A_{q}^{(3)} = C_{11}\left[\frac{1}{16}\gamma_{14}\gamma_{24}\left(\frac{m^{4}}{\gamma_{7}} + \frac{n^{4}\beta^{4}}{\gamma_{6}}\right) - \gamma_{14}(m^{2}B_{200}\right)\right],$$

$$+n^{2}\beta^{2}b_{200},$$

in which (other symbols are defined as in ref. [41])

(A.3)
$$C_{11} = \frac{\pi^{2}}{16}mn, \ \Theta_{3} = \alpha_{313} + \alpha_{331},$$

$$\alpha_{313} = \frac{1}{16}\gamma_{14}\gamma_{24}\frac{m^{4}}{\gamma_{7}G_{138}}, \ \alpha_{331} = \frac{1}{16}\gamma_{14}\gamma_{24}\frac{n^{4}\beta^{4}}{\gamma_{6}G_{318}},$$

$$G_{08} = g_{08} + \gamma_{14}\gamma_{24}\frac{g_{07}^{*}g_{05}^{*}}{g_{06}} + [K_{1} + K_{2}(m^{2} + n^{2}\beta^{2})]$$

$$- \gamma_{14}(m^{2}B_{000} + n^{2}\beta^{2}b_{000})$$

$$- \frac{32}{3\pi^{2}}\gamma_{14}\gamma_{24}m^{2}n^{2}\beta^{2}\frac{g_{01}^{*}}{g_{06}}\frac{16}{\pi^{2}}\Delta T\frac{h}{[D_{11}^{*}D_{22}^{*}A_{11}^{*}A_{22}^{*}]^{1/4}},$$
(B.2)
$$(A.4) \quad G_{138} = g_{138} + \gamma_{14}\gamma_{24}\frac{g_{137}^{*}g_{135}^{*}}{g_{136}} + [K_{1} + K_{2}(m^{2} + 9n^{2}\beta^{2})]$$

$$- \gamma_{14}(m^{2}B_{000} + 9n^{2}\beta^{2}b_{000}),$$

$$G_{318} = g_{318} + \gamma_{14}\gamma_{24}\frac{g_{317}^{*}g_{315}^{*}}{g_{316}} + [K_{1} + K_{2}(9m^{2} + n^{2}\beta^{2})]$$

$$- \gamma_{14}(9m^{2}B_{000} + n^{2}\beta^{2}b_{000}),$$

in the above equations, B_{000} , b_{000} , B_{200} , and b_{200} are the same as defined in equations (A.5) and (A.6).